On-Chip Terahertz Spectroscopy for Dual-Gated van der Waals Heterostructures at Cryogenic Temperatures

Junseok Seo,[1] Zhengguang Lu,[1] Jixiang Yang,[1] Fangzhou Xia,[1,2] Shenyong Ye,[1] Yuxuan Yao,[1] Tonghang Han,[1] Lihan Shi,[1] Kenji Watanabe,[3] Takashi Taniguchi,[4] and Long Ju*[,1]

[1]Department of Physics, Massachusetts Institute of Technology, Cambridge, MA 02139, USA
[2]Department of Mechanical Engineering, Massachusetts Institute of Technology, Cambridge, MA 02139, USA
[3]Research Center for Electronic and Optical Materials, National Institute for Materials Science, 1-1 Namiki, Tsukuba 305-0044, Japan
[4]Research Center for Materials Nanoarchitectonics, National Institute for Materials Science, 1-1 Namiki, Tsukuba 305-0044, Japan

*Corresponding author. Email: longju@mit.edu

Abstract

Van der Waals heterostructures have emerged as a versatile platform to study correlated and topological electron physics. Spectroscopy experiments in the THz regime are crucial, since the energy of THz photons matches that of relevant excitations and charge dynamics. However, their micron-size and complex (dual-)gated structures have challenged such measurements. Here, we demonstrate on-chip THz spectroscopy on a dual-gated bilayer graphene device at liquid helium temperature. To avoid unwanted THz absorption by metallic gates, we developed a scheme of operation by combining semiconducting gates and optically controlled gating. This allows us to measure the clean THz response of graphene without being affected by the gates. We observed the THz signatures of electric-field-induced bandgap opening at the charge neutrality. We measured Drude conductivities at varied charge densities and extracted key parameters, including effective masses and scattering rates. This work paves the way for studying novel emergent phenomena in dual-gated two-dimensional materials.

KEYWORDS: Terahertz time-domain spectroscopy, van der Waals heterostructure, dual gate, optical conductivity, graphene

Van der Waals (vdW) heterostructures of two-dimensional (2D) materials have emerged as a powerful platform to study physics of electron correlation and topology.[1,2] Lots of intriguing ground states have been discovered thanks to various tuning knobs available to this material system, such as composition, stacking order, electrostatic gating, and twist angle.[3-23] To understand the underlying physics of these emergent quantum phenomena, information gained through spectroscopy experiments is needed in addition to electrical transport measurements. However, many conventional spectroscopy techniques cannot be directly applied to this new material system due to mainly two challenges. Firstly, most of the systems require a dual-gated structure, where a top gate and encapsulating dielectric prevent surface probes such as scanning tunneling microscopy and photo-emission spectroscopy from exploring the full phase space controlled by the charge density and the gate electric field.[24-27] Secondly, the relevant energy scale of the electron correlation is much smaller than that of conventional strongly correlated materials. For instance, the lattice period of moiré superlattices much larger than atomic bond lengths in crystals results in smaller energy scales for their emergent phenomena. For optical spectroscopy, directly probing excitations in 2D heterostructures requires the application of photons with wavelength (hundreds to thousands of microns) much larger than the typical size of high-quality devices (~10 μm). The Fourier-transformed infrared photocurrent spectroscopy partially overcame these issues,[28-30] but it cannot be directly applied to metallic states due to the large current noise.

On-chip terahertz (THz) spectroscopy has been demonstrated as an effective technique to study low-energy electron dynamics in micron-sized 2D materials (1 THz = 4.14 meV).[31,32] Different from far-field THz spectroscopy, the on-chip configuration confines the THz electric field between a pair of metal transmission lines to efficiently couple to 2D material flakes. Although it has been employed to study monolayer graphene, superconducting NbN and K_3C_{60},[31-34] applying the same technique to dual-gated vdW heterostructures faces significant additional challenges, especially at liquid helium temperature which is often required for revealing the electron correlation effect in vdW heterostructures. Firstly, a metallic top gate may screen the THz electric field and mask the signal from the underlying material of interest. Secondly, although one can potentially reduce the gate disturbance by using a poorly conducting gate layer such as semiconducting transition metal dichalcogenides (TMDs), this scheme has not been demonstrated at liquid helium temperature due to a dilemma: charges in semiconducting TMDs tend to be frozen at liquid helium temperature due to the metal-insulator transition,[35,36] but using a metallic TMD layer could result in DC and THz conductivities similar to or higher than the layer of interest, for example, magic-angle twisted bilayer graphene (see Section S1 in the Supporting Information for detailed discussions).[3,37]

Here, we devise a novel scheme to tame these obstacles by optically activating and deactivating semiconducting TMDs. We show that TMDs can act as a gate when they become photo-conductive, even when they are originally insulating. After the optical illumination to activate the gates is turned off, charges at both TMD gates and a sample layer of interest are maintained. Importantly, the mobility of charges in the gate layers is greatly reduced in the dark

environment and their contribution to THz absorption becomes negligible. We demonstrated this scheme by using dual-gated Bernal-stacked bilayer graphene (BLG) as an example, where we measured the dynamic responses of its Fermi liquids.

We fabricated a device (see Section S2 for the procedure) as illustrated in Figure 1a. On a fused silica substrate, the THz emitter, the dual-gated BLG stack, and the THz receiver are dispersed along a pair of transmission lines. The emitter and receiver are photo-conductive switches based on GaAs. THz pulses are launched by femtosecond-laser-excited carriers in the emitter and detected by the receiver in the form of photocurrent. The electric field of THz pulses are recorded as a function of time delay, which can be later transformed into a frequency domain to reveal the spectrum (see Section S3 for the details of THz measurements). When transmitting through the BLG stack, the THz electric field is reduced due to the absorption, and the transmitted THz signal can be used to extract the optical conductivity spectrum of the stack. In our device, the absorption and conductivity are modulated by the charge density and gate electric field by controlling the back and top gate voltages, V_{BG} and V_{TG}. In contrast to previous studies, one important new component in our configuration is a white light (WL) illumination that will be used to modulate the electric properties of the semiconducting gate layers.

Figure 1b shows the details of the BLG stack, where two WS_2 flakes serve as the gate layers. The THz waveguide is separated from the BLG stack by the hBN dielectrics. Electrodes are deposited for controlling the electrostatic potentials of BLG and gate layers. We used few-layer graphite flakes to bridge the WS_2 flakes and the gold electrodes.

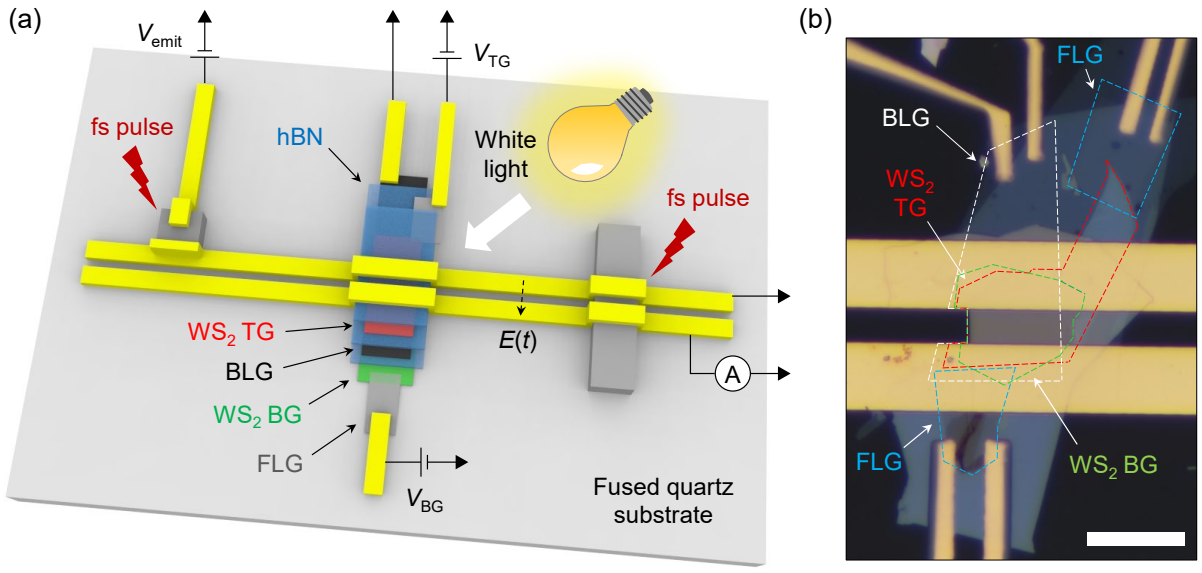

Figure 1. Device structure and measurement scheme. *(a) Schematic of our device and measurement setup from a top view. BG, TG, and FLG denote back gate, top gate, and few-layer graphite, respectively. A current pulse generated in the waveguide by the emitter generates a THz electric field. The transmitted electric field after going through the sample and traveling the*

waveguide is received by the receiver. White light illumination is used to activate the TMD gates. ***(b)*** *Optical micrograph of our dual-gated BLG device BLG1 embedded in the waveguide. The flakes are outlined by dashed lines with corresponding color. Scale bar, 20 μm.*

The key to a reliable measurement of the BLG THz conductivity is to suppress the free-charge-carrier contribution from the gate layers. This is a dilemma, however, since the mobile charges that supply the gate electric field will unavoidably absorb THz pulses in the static gating scheme and mislead the true absorption by BLG only (see Section S4 for the THz measurements performed with a conducting back gate). We now demonstrate a scheme to solve this problem by combining light illumination, application of gate voltages, and defect/impurity states in WS_2. We purposely choose WS_2 as the gate, which remains insulating in a wide range of gate voltage at liquid helium temperature.[36] As a result, the gate cannot function in the dark environment due to the lack of free carriers. This is shown as the blue curve in Figure 2a, in which the transmitted photocurrent signal remains as a constant while the gate voltage is scanned. To activate the gate, we can illuminate it using WL and excite free carriers in WS_2. A certain range of WL's photon wavelength is chosen so that it can trigger the photon absorption of WS_2 and avoid photo-induced doping effect simultaneously (see Section S3).[38,39] As a result, the transmitted photocurrent signal now responses to the sweeping gate, as shown in the orange curve in Figure 2a. At $V_{BG} = -0.6$ V, the current reaches a maximum, which corresponds to when BLG is in the charge-neutral state. Here, we fix the time delay t at when the photocurrent across the receiver, $I_x(t)$, reaches a positive maximal value, and define this time delay as $t = 0$ as shown in the inset of Figure 2a.

Performing THz measurements with the WL turned on, however, is problematic for several reasons: 1. The photo-excited free carriers in the WS_2 gate will absorb the THz pulse and this absorption varies with the gate voltage. Correspondingly, the extraction of the THz response from the BLG will be misinterpreted, and the problem will be even more severe for 2D flat-band systems due to their smaller Drude conductivity; 2. The WL illumination could excite and heat up the BLG, resulting in the measured response being different from the ground state of BLG. To overcome these issues, we developed a procedure that is composed of three steps as shown in Figure 2b and 2c. The left and middle panel in both Figure 2b and 2c illustrate how the WS_2 gate and BLG respond to gate voltages when WL is turned off and on, as we have explained above. After the charges settle down in both the WS_2 gate and BLG, we can turn off the WL as shown in the third column of Figure 2b and 2c. In the final state with WL off, the photo-excited free carriers in WS_2 in the second step get trapped at defect/impurity states. The key point here is that these trapped charges contribute to negligible THz absorption but can keep the gating effect persisting even after turning off the WL. We tested this scheme with other BLG devices (see Section S5 and S6). As a result, we showed the reproducibility of our gating method and confirmed that doped charges can persist for 30 minutes at least. Although the obtained value of persisting time was limited by measurement time, it was still long enough for practical THz measurements.

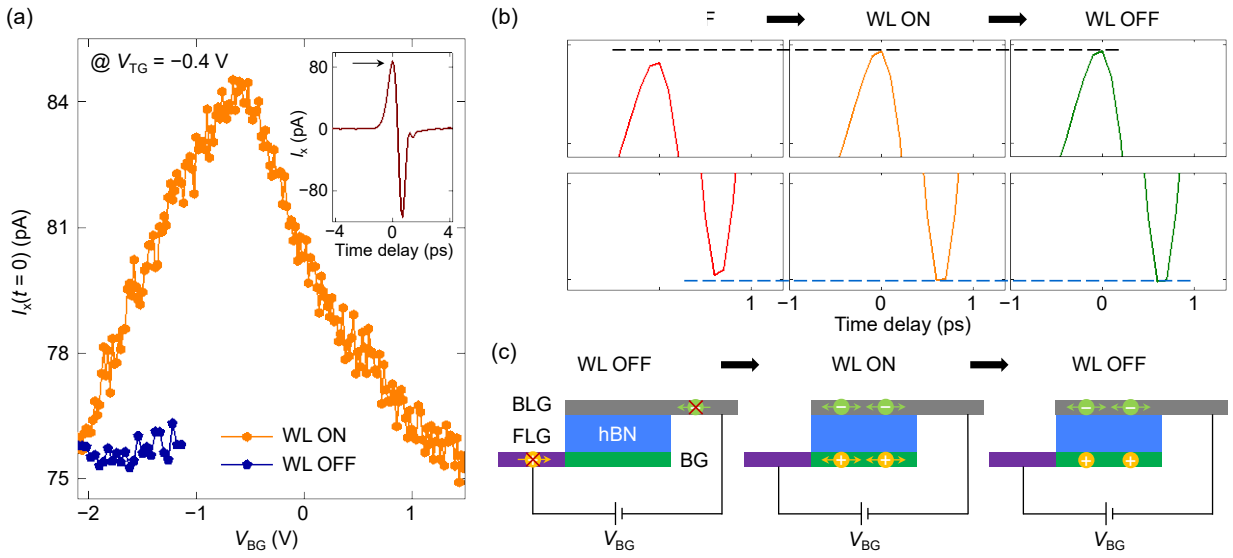

Figure 2. Optical activation of semiconducting TMD gates at T = 2.5 K. *(**a**) Comparison of gating with and without WL. When the WL was turned on, gate voltages were set to be V_{BG} = −2.1 V and V_{TG} = −0.4 V. Afterwards, V_{BG} was swept to 1.5 V when the WL was turned on (yellow) or off (navy), and $I_x(t = 0)$ was recorded. Inset: Representative time-domain current I_x data. (**b**) Change in a transmitted THz field as the WL is turned on and off again. Gate voltages were set to be V_{BG} = 2 V and V_{TG} = −1 V when the WL was turned off, and then the time-domain current I_x was recorded (red). Then, the WL was turned on and then I_x was measured (yellow). Subsequently, I_x was measured again after the WL was turned off (green). The maximum positive and negative current were identical for the yellow and green curve (black and blue dotted line, respectively), which showed clear difference from that of the red curve. (**c**) Illustrations of charges in BLG and back gate (BG) layer in the sequence of (**b**). When the WL is turned off (left), charges cannot be injected to the BG and BLG layer since the BG is too insulating. When the WL is turned on (middle), charges are injected and are mobile (represented by double-sided arrows). When the WL is off again (right), charges in the BG layer are frozen and thus cannot contribute to THz absorption.*

Using this gating procedure, we now examine the transmitted THz pulses as a function of charge density n and gate displacement field D which are controlled by the combination of V_{BG} and V_{TG}. Before performing the THz measurement at specific n and D to extract the optical conductivity spectrum, we need to understand the basic band structure and experimentally determine the relation between (V_{BG}, V_{TG}) and (n, D). Figure 3a shows the current $I_x(t = 0)$ going through the THz receiver as a function of V_{BG} and V_{TG}. We observed a bright stripe, which corresponds to increased $I_x(t = 0)$, in the diagonal direction as traced by the red dashed line. In the direction orthogonal to this line, the $I_x(t = 0)$ signal decreases away from the points on the dashed line. Along the dashed line, $I_x(t = 0)$ shows a minimum at the point indicated by the black arrow.

We can understand the $I_x(t = 0)$ map based on the previous studies of the BLG band structure.[40,41] As illustrated in Figure 3b, at $n = D = 0$, BLG is in a charge-neutral state with zero bandgap. In this case, the interband optical transitions result in some THz absorption as represented by vertical arrows in the left panel of Figure 3b. Starting from this scenario, fixing at charge neutrality and increasing $|D|$ will open up a bandgap, which suppresses the interband transition and gives rise to an increase in $I_x(t = 0)$. These expectations agree with the observed $I_x(t = 0)$ signals along the red dashed line in Figure 3a, and the black arrow indicating the $n = D = 0$ point. Fixing D and increasing $|n|$ will induce intraband transitions corresponding to the doped charge carriers, and results in more THz absorption and a decrease in $I_x(t = 0)$. These expectations agree with the observed $I_x(t = 0)$ signals along the orthogonal direction of the red dashed line in Figure 3a.

With this qualitative picture in mind, we try to quantitatively define the relation between (V_{BG}, V_{TG}) and (n, D). Figure 3c shows a line-cut along the black dotted line in Figure 3a at varying temperatures. In each curve, the maximal value of $I_x(t = 0)$ corresponds to $n = 0$, i.e., the charge-neutral point (CNP). The determination of V_{TG} corresponding to the CNP becomes more accurate at lower temperatures, as the peak becomes sharper due to reduced thermal fluctuations. For each V_{BG}, the corresponding V_{TG} to get CNP can be determined in this way shown in Figure 3c. Repeating this procedure for several V_{BG} values, we can obtain all the CNPs through linear fitting, as shown in Figure 3d. We further determine (n, D) from (V_{BG}, V_{TG}) through the analysis of gate capacitances (see Section S7).

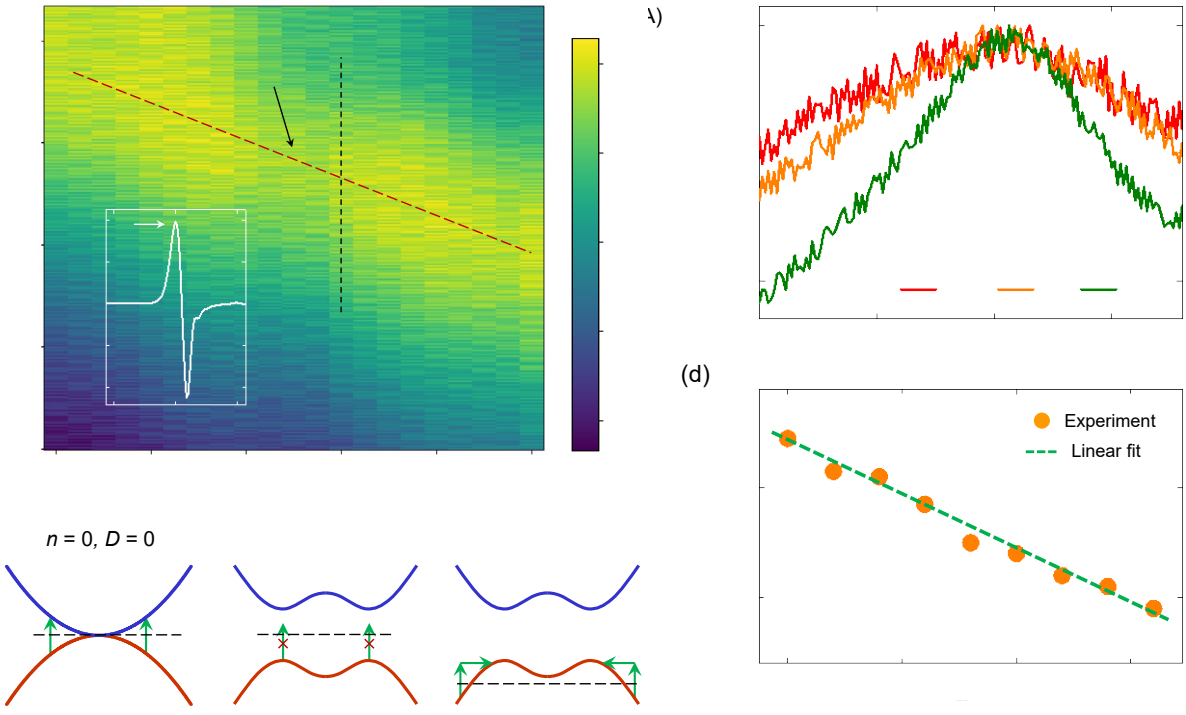

Figure 3. Optical determination of BLG's CNP. *(a) Time-domain current I_x at the time delay of zero (white arrow in the inset) as a function of gate voltages. The red dotted line denotes the local*

*maximum of $I_x(t = 0)$ and a point where $I_x(t = 0)$ is minimum along this line is attributed to $D = 0$ CNP (black arrow). (**b**) Schematic illustrations of low-energy BLG band structures that show BLG's THz absorption. When $n = 0$ and $D = 0$ (left), some THz pulse can be absorbed by interband transitions. When $n = 0$ and $D \neq 0$ (middle), a bandgap at CNP is open and THz absorption by interband transitions is suppressed. When $n \neq 0$ (right), intraband transitions give rise to THz absorption. (**c**) Relationship between $I_x(t = 0)$ normalized by its maximum value and V_{TG} for $V_{BG} = 0.3$ V, taken at three different temperatures. The corresponding line-cut in (**a**) is shown there as a black dotted line. (**d**) Relation between V_{BG} and V_{TG} corresponding to maximum $I_x(t = 0)$ from the experimental data (yellow) and its linear fit (green).*

We now turn to the measurements of complex optical conductivity spectra at independently controlled n and D. Assuming the THz absorption by WS_2 gates can be neglected due to our new scheme of gating as described in Figure 2, the next issue to solve is to find a good reference THz signal to mimic the incident THz pulse totally unaffected by the BLG stack. For far-field THz spectroscopy, the reference signal can be obtained by removing the sample. However, a sample cannot be taken out from our device structure without disturbing the waveguide. Instead, we use the THz signal obtained at $D/\varepsilon_0 = 80$ mV/nm and $n = 0$ cm^{-2} as the reference, since the bandgap is big enough to suppress all inter-band transitions and the intra-band transitions cannot happen at zero charge density.[28]

We collected the time-domain current I_x at this reference condition and at $n = -0.6, -0.9, -1.2 \times 10^{12}$ cm^{-2} and $D/\varepsilon_0 = 60$ mV/nm, as shown in Figure 4a. Similar measurements were done for $n = -0.6, -0.9, -1.2 \times 10^{12}$ cm^{-2} and $D/\varepsilon_0 = 20$ mV/nm (Figure 4b). For the fixed D, the $I_x(t = 0)$ signal decreases as n increased, suggesting the change is dominated by the intraband transitions.

To extract the spectrum as a function of frequency f, we first perform Fourier transformation to obtain both the reference $\epsilon_{\mathrm{ref}}(\omega = 2\pi f)$ and the signal $\epsilon(\omega)$ in the frequency domain. Then, we calculate the optical conductivity as $\sigma(\omega) = \sigma_1(\omega) - i\sigma_2(\omega) = \frac{2W}{Z_0 d}\left[\frac{\epsilon_{\mathrm{ref}}(\omega)}{\epsilon(\omega)} - 1\right]$, which is derived from waveguide electrodynamics.[31] Here, $Z_0 = 126\ \Omega$ is the characteristic impedance of the waveguide obtained from simulations (see Section S8), $W = 8$ μm is the gap between the two metal lines of the transmission line, and $d = 21$ μm is the length of BLG along the waveguide direction. This approach compensates for intrinsic and extrinsic effects that may affect the faithful extraction of optical conductivities, such as the frequency-dependent intensity of the generated THz field and the dispersion of a THz pulse during its propagation along the waveguide.

The calculated optical conductivity is shown in Figure 4c and 4d. The data were fitted by the Drude model $\sigma(\omega) = \frac{D^*}{\pi}\frac{1}{\tau^{-1} + i\omega}$, where D^* is Drude weight and τ is relaxation time. Here, the data are demonstrated up to the frequency of 1.2 THz due to the bandwidth of our THz pulse (see Section S9). The experimental data follows the model-predicted curves quite well across the whole frequency range, proving the effectiveness of our WL-controlled gating scheme.

The Drude weight is expressed as $D^* = \pi n e^2/m$, where m is the effective mass of charge carriers in BLG. In this regard, we could extract m and τ at each combination of n and D (see Section S10). The values of m fall into the range of $0.040 - 0.048 m_0$, where m_0 is the mass of a bare electron. These are consistent with previous quantum oscillation measurement results.[42-44] We further extract the charge mobility to be of around 56000 $cm^2\ V^{-1}\ s^{-1}$, thanks to the simultaneous and independent extractions of m and τ. The obtained mobility supports the value of studying a clean micron-scale hBN-encapsulated sample, rather than exfoliated graphene on SiO_2 and large-area graphene grown by chemical vapor deposition.[45,46]

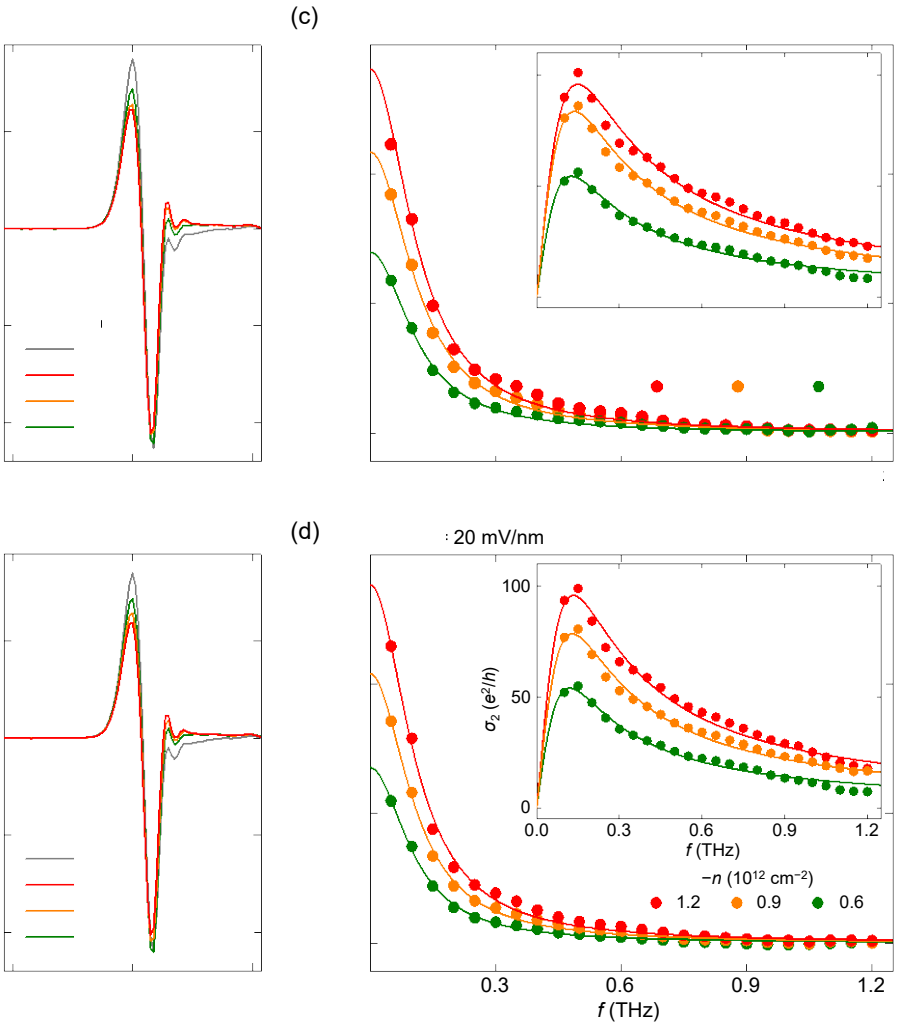

Figure 4. Optical conductivity spectra of Fermi liquids at T = 2.5 K and varied n and D. *Representative time-domain current I_x measured at charge density $n = -0.6$ (red), -0.9 (yellow), -1.2 (green) $\times 10^{12}$ cm^{-2} at **(a)** $D/\varepsilon_0 = 60$ mV/nm and **(b)** $D/\varepsilon_0 = 20$ mV/nm. The reference (Ref, grey) was taken at CNP, $D/\varepsilon_0 = 80$ mV/nm. Corresponding spectra of σ_1 and σ_2 at **(c)** $D/\varepsilon_0 = 60$ mV/nm and **(d)** $D/\varepsilon_0 = 20$ mV/nm. Dots are the experimental data calculated from **(a)** and **(b)**, and lines are fits to the Drude model.*

In summary, we have developed a light-controlled gating scheme for performing the on-chip THz spectroscopy experiment on dual-gated 2D heterostructure devices at and below the liquid helium temperature. This new gating scheme strongly suppresses contribution to THz absorption by the gate layers and allows us to obtain clean optical conductivity spectra in BLG that agree nicely with the Drude model. In this scheme, the carrier density and displacement field could be tuned independently to measure and compare the properties of different ground states of the device. Our work opens up a lot of exciting opportunities for spectroscopic studies on correlated and topological physics in 2D vdW heterostructures, especially in two directions. Firstly, our technique can directly probe charge gaps in the sub-meV to a-few-meV range, where the energy gap of many interesting ground states such as superconductors and fractional Chern insulators are expected to reside.[23-25] Secondly, it can be utilized to investigate the charge dynamics of diverse compressible states. THz spectroscopy has been employed to study unconventional metallic states such as non-Fermi liquids,[47] whose signatures have recently been observed in vdW systems as well.[16,48,49] More recently, composite-fermion-like behavior has been observed in a half-filled flat Chern band at zero magnetic field.[20,22] THz spectroscopy could provide valuable insights into such new emergent quantum phenomena. Technically, the on-chip THz spectroscopy covers the right frequency range that corresponds to the relaxation time in graphene and other clean 2D materials. Beyond THz measurements, our gating scheme could be generalized to other advanced spectroscopy and microscopy experiments such as a scanning single-electron transistor and microwave impedance microscopy,[50,51] which are important techniques for understanding the underlying physics of dual-gated vdW heterostructures.

References

1. Andrei, E. Y.; Efetov, D. K.; Jarillo-Herrero, P.; MacDonald, A. H.; Mak, K. F.; Senthil, T.; Tutuc, E.; Yazdani, A.; Young, A. F. The Marvels of Moiré Materials. *Nat. Rev. Mater.* **2021**, 6, 201-206.
2. Pantaleón, P. A.; Jimeno-Pozo, A.; Sainz-Cruz, H.; Phong, V. T.; Cea, T.; Guinea, F. Superconductivity and Correlated Phases in Non-Twisted Bilayer and Trilayer Graphene. *Nat. Rev. Phys.* **2023**, 5, 304-315.
3. Cao, Y.; Fatemi, V.; Fang, S.; Watanabe, K.; Taniguchi, T.; Kaxiras, E.; Jarillo-Herrero, P. Unconventional Superconductivity in Magic-Angle Graphene Superlattices. *Nature* **2018**, 556, 43-50.
4. Park, J. M.; Cao, Y.; Watanabe, K.; Taniguchi, T.; Jarillo-Herrero, P. Tunable Strongly Coupled Superconductivity in Magic-Angle Twisted Trilayer Graphene. *Nature* **2021**, 590, 249-225.
5. Hao, Z.; Zimmerman, A. M.; Ledwith, P.; Khalaf, E.; Najafabadi, D. H.; Watanabe, K.; Taniguchi, T.; Viswanath, A.; Kim, P. Electric Field-Tunable Superconductivity in Alternating-Twist Magic-Angle Trilayer Graphene. *Science* **2021**, 371, 1133-1138.

6. Park, J. M.; Cao, Y.; Xia, L.-Q.; Sun, S.; Watanabe, K.; Taniguchi, T.; Jarillo-Herrero, P. Robust Superconductivity in Magic-Angle Multilayer Graphene Family. *Nat. Mater.* **2022**, 21, 877-883.
7. Zhang, Y.; Polski, R.; Lewandowski, C.; Thomson, A.; Peng, Y.; Choi, Y.; Kim, H.; Watanabe, K.; Taniguchi, T.; Alicea, J.; von Oppen, F.; Refael, G.; Nadj-Perge, S. Promotion of Superconductivity in Magic-Angle Graphene Multilayers. *Science* **2022**, 377, 1538-1543.
8. Zhou, H.; Xie, T.; Taniguchi, T.; Watanabe, K.; Young, A. F. Superconductivity in Rhombohedral Trilayer Graphene. *Nature* **2021**, 598, 434-438.
9. Zhou, H.; Holleis, L.; Saito, Y.; Cohen, L.; Huynh, W.; Patterson, C. L.; Yang, F.; Taniguchi, T.; Watanabe, K.; Young, A. F. Isospin Magnetism and Spin-Polarized Superconductivity in Bernal Bilayer Graphene. *Science* **2022**, 375, 774-778.
10. Zhang, Y.; Polski, R.; Thomson, A.; Lantagne-Hurtubise, É.; Lewandowski, C.; Zhou, H.; Watanabe, K.; Taniguchi, T.; Alicea, J.; Nadj-Perge, S. Enhanced Superconductivity in Spin-Orbit Proximitized Bilayer Graphene. *Nature* **2023**, 613, 268-273.
11. Cao, Y.; Fatemi, V.; Demir, A.; Fang, S.; Tomarken, S. L.; Luo, J. Y.; Sanchez-Yamagishi, J. D.; Watanabe, K.; Taniguchi, T.; Kaxiras, E.; Ashoori, R. C.; Jarillo-Herrero, P. Correlated Insulator Behaviour at Half-Filling in Magic-Angle Graphene Superlattices. *Nature* **2018**, 556, 80-84.
12. Chen, G.; Jiang, L.; Wu, S.; Lyu, B.; Li, H.; Chittari, B. L.; Watanabe, K.; Taniguchi, T.; Shi, Z.; Jung, J.; Zhang, Y.; Wang, F. Evidence of a Gate-Tunable Mott Insulator in a Trilayer Graphene Moiré Superlattice. *Nat. Phys.* **2019**, 15, 237-241.
13. Wang, L.; Shih, E.-M.; Ghiotto, A.; Xian, L.; Rhodes, D. A.; Tan, C.; Claassen, M.; Kennes, D. M.; Bai, T.; Kim, B.; Watanabe, K.; Taniguchi, T.; Zhu, X.; Hone, J.; Rubio, A.; Pasupathy, A. N.; Dean, C. R. Correlated Electronic Phases in Twisted Bilayer Transition Metal Dichalcogenides. *Nat. Mater.* **2020**, 19, 861-866.
14. Han, T.; Lu, Z.; Scuri, G.; Sung, J.; Wang, J.; Han, T.; Watanabe, K.; Taniguchi, T.; Park, H.; Ju, L. Correlated Insulator and Chern Insulators in a Pentalayer Rhombohedral-Stacked Graphene. *Nat. Nanotechnol.* **2024**, 19, 181-187.
15. Liu, K.; Zheng, J.; Sha, Y.; Lyu, B.; Li, F.; Park, Y.; Ren, Y.; Watanabe, K.; Taniguchi, T.; Jia, J.; Luo, W.; Shi, Z.; Jung, J.; Chen, G. Spontaneous Broken-Symmetry Insulator and Metals in Tetralayer Rhombohedral Graphene. *Nat. Nanotechnol.* **2024**, 19, 188-195.
16. Ghiotto, A.; Shih, E.-M.; Pereira, G. S. S. G.; Rhodes, D. A.; Kim, B.; Zang, J.; Millis, A. J.; Watanabe, K.; Taniguchi, T.; Hone, J.; Wang, L.; Dean, C. R.; Pasupathy, A. N. Quantum Criticality in Twisted Transition Metal Dichalcogenides. *Nature* **2021**, 597, 345-349.
17. Serlin, M.; Tschirhart, C. L.; Polshyn, H.; Zhang, Y.; Zhu, J.; Watanabe, K.; Taniguchi, T.; Balents, L.; Young, A. F. Intrinsic Quantized Anomalous Hall Effect in a Moiré Heterostructure. *Science* **2020**, 367, 900-903.
18. Li, T.; Jiang, S.; Shen, B.; Zhang, Y.; Li, L.; Tao, Z.; Devakul, T.; Watanabe, K.; Taniguchi, T.; Fu, L.; Shan, J.; Mak, K. F. Quantum Anomalous Hall Effect from Intertwined Moiré Bands. *Nature* **2021**, 600, 641-646.

19. Han, T.; Lu, Z.; Yao, Y.; Yang, J.; Seo, J.; Yoon, C.; Watanabe, K.; Taniguchi, T.; Fu, L.; Zhang, F.; Ju, L. Large Quantum Anomalous Hall Effect in Spin-Orbit Proximitized Rhombohedral Graphene. *Science* **2024**, 384, 647-651.
20. Park, H.; Cai, J.; Anderson, E.; Zhang, Y.; Zhu, J.; Liu, X.; Wang, C.; Holtzmann, W.; Hu, C.; Liu, Z.; Taniguchi, T.; Watanabe, K.; Chu, J.-H.; Cao, T.; Fu, L.; Yao, W.; Chang, C.-Z.; Cobden, D.; Xiao, D.; Xu, X. Observation of Fractionally Quantized Anomalous Hall Effect. *Nature* **2023**, 622, 74-79.
21. Xu, F.; Sun, Z.; Jia, T.; Liu, C.; Xu, C.; Li, C.; Gu, Y.; Watanabe, K.; Taniguchi, T.; Tong, B.; Jia, J.; Shi, Z.; Jiang, S.; Zhang, Y.; Liu, X.; Li, T. Observation of Integer and Fractional Quantum Anomalous Hall Effects in Twisted Bilayer $MoTe_2$. *Phys. Rev. X* **2023**, 13, 031037.
22. Lu, Z.; Han, T.; Yao, Y.; Reddy, A. P.; Yang, J.; Seo, J.; Watanabe, K.; Taniguchi, T.; Fu, L.; Ju, L. Fractional Quantum Anomalous Hall Effect in Multilayer Graphene. *Nature* **2024**, 626, 759-764.
23. Zeng, Y.; Xia, Z.; Kang, K.; Zhu, J.; Knüppel, P.; Vaswani, C.; Watanabe, K.; Taniguchi, T.; Mak, K. F. Shan, J. Thermodynamic Evidence of Fractional Chern Insulator in Moiré $MoTe_2$. *Nature* **2023**, 622, 69-73.
24. Oh, M.; Nuckolls, K. P.; Wong, D.; Lee, R. L.; Liu, X.; Watanabe, K.; Taniguchi, T.; Yazdani, A. Evidence for Unconventional Superconductivity in Twisted Bilayer Graphene. *Nature* **2021**, 600, 240-245.
25. Kim, H.; Choi, Y.; Lewandowski, C.; Thomson, A.; Zhang, Y.; Polski, R.; Watanabe, K.; Taniguchi, T.; Alicea, J.; Nadj-Perge, S. Evidence for Unconventional Superconductivity in Twisted Trilayer Graphene. *Nature* **2022**, 606, 494-500.
26. Utama, M. I. B.; Koch, R. J.; Lee, K.; Leconte, N.; Li, H.; Zhao, S.; Jiang, L.; Zhu, J.; Watanabe, K.; Taniguchi, T.; Ashby, P. D.; Weber-Bargioni, A.; Zettl, A.; Jozwiak, C.; Jung, J.; Rotenberg, E.; Bostwick, A.; Wang, F. Visualization of the Flat Electronic Band in Twisted Bilayer Graphene near the Magic Angle Twist. *Nat. Phys.* **2021**, 17, 184-188.
27. Lisi, S.; Lu, X.; Benschop, T.; de Jong, T. A.; Stepanov, P.; Duran, J. R.; Margot, F.; Cucchi, I.; Cappelli, E.; Hunter, A.; Tamai, A.; Kandyba, V.; Giampietri, A.; Barinov, A.; Jobst, J.; Stalman, V.; Leeuwenhoek, M.; Watanabe, K.; Taniguchi, T.; Rademaker, L.; van der Molen, S. J.; Allan, M. P.; Efetov, D. K.; Baumberger, F. Observation of Flat Bands in Twisted Bilayer Graphene. *Nat. Phys.* **2021**, 17, 189-193.
28. Ju, L.; Wang, L.; Cao, T.; Taniguchi, T.; Watanabe, K.; Louie, S. G.; Rana, F.; Park, J.; Hone, J.; Wang, F.; McEuen, P. L. Tunable Excitons in Bilayer Graphene. *Science* **2017**, 358, 907-910.
29. Han, T.; Yang, J.; Zhang, Q.; Wang, L.; Watanabe, K.; Taniguchi, T.; McEuen, P. L.; Ju, L. Accurate Measurement of the Gap of Graphene/*h*-BN Moiré Superlattice through Photocurrent Spectroscopy. *Phys. Rev. Lett.* **2021**, 126, 146402.
30. Yang, J.; Chen, G.; Han, T.; Zhang, Q.; Zhang, Y.-H.; Jiang, L.; Lyu, B.; Li, H.; Watanabe, K.; Taniguchi, T.; Shi, Z.; Senthil, T.; Zhang, Y.; Wang, F.; Ju, L. Spectroscopy Signatures of

Electron Correlations in a Trilayer Graphene/hBN Moiré Superlattice. *Science* **2022**, 375, 1295-1299.
31. Gallagher, P.; Yang, C.-S.; Lyu, T.; Tian, F.; Kou, R.; Zhang, H.; Watanabe, K.; Taniguchi, T.; Wang, F. Quantum-Critical Conductivity of the Dirac Fluid in Graphene. *Science* **2019**, 364, 158-162.
32. Zhao, W.; Wang, S.; Chen, S.; Zhang, Z.; Watanabe, K.; Taniguchi, T.; Zettl, A.; Wang, F. Observation of Hydrodynamic Plasmons and Energy Waves in Graphene. *Nature* **2023**, 614, 688-693.
33. Potts, A. M.; Nayak, A. K.; Nagel, M.; Kaj, K.; Stamenic, B.; John, D. D.; Averitt, R. D.; Young, A. F. On-Chip Time-Domain Terahertz Spectroscopy of Superconducting Films below the Diffraction Limit. *Nano Lett.* **2023**, 23, 3835-3841.
34. Wang, E.; Adelinia, J. D.; Chavez-Cervantes, M.; Matsuyama, T.; Fechner, M.; Buzzi, M.; Meier, G.; Cavalleri, A. Superconducting Nonlinear Transport in Optically Driven High-Temperature K_3C_{60}. *Nat. Commun.* **2023**, 14, 7233.
35. Radisavljevic, B.; Kis, A. Mobility Engineering and a Metal-Insulator Transition in Monolayer MoS_2. *Nat. Mater.* **2013**, 12, 815-820.
36. Ovchinnikov, D.; Allain, A.; Huang, Y.-S.; Dumcenco, D.; Kis, A. Electrical Transport Properties of Single-Layer WS_2. *ACS Nano* **2014**, 8, 8174-8181.
37. Cui, X.; Lee, G.-H.; Kim, Y. D.; Arefe, G.; Huang, P. Y.; Lee, C.-H.; Chenet, D. A.; Zhang, X.; Wang, L.; Ye, F.; Pizzocchero, F.; Jessen, B. S.; Watanabe, K.; Taniguchi, T.; Muller, D. A.; Low, T.; Kim, P.; Hone, J. Multi-Terminal Transport Measurements of MoS_2 Using a van der Waals Heterostructure Device Platform. *Nat. Nanotechnol.* **2015**, 10, 534-540.
38. Ju, L.; Velasco Jr, J.; Huang, E.; Kahn, S.; Nosiglia, C.; Tsai, H.-Z.; Yang, W.; Taniguchi, T.; Watanabe, K.; Zhang, Y.; Zhang, G.; Crommie, M.; Zettl, A.; Wang, F. Photoinduced Doping in Heterostructures of Graphene and Boron Nitride. *Nat. Nanotechnol.* **2014**, 9, 348-352.
39. Zhao, W.; Ghorannevis, Z.; Chu, L.; Toh, M.; Kloc, C.; Tan, P.-H.; Eda, G. Evolution of Electronic Structure in Atomically Thin Sheets of WS_2 and WSe_2. *ACS Nano* **2013**, 7, 791-797.
40. Zhang, Y.; Tang, T.-T.; Girit, C.; Hao, Z.; Martin, M. C.; Zettl, A.; Crommie, M. F.; Shen, Y. R.; Wang, F. Direction Observation of a Widely Tunable Bandgap in Bilayer Graphene. *Nature* **2009**, 459, 820-823.
41. Mak, K. F.; Lui, C. H.; Shan, J.; Heinz, T. F. Observation of an Electric-Field-Induced Band Gap in Bilayer Graphene by Infrared Spectroscopy. *Phys. Rev. Lett.* **2009**, 102, 256405.
42. Castro, E. V.; Novoselov, K. S.; Morozov, S. V.; Peres, N. M. R.; Lopes dos Santos, J. M. B.; Nilsson, J.; Guinea, F.; Geim, A. K.; Castro Neto, A. H.; Biased Bilayer Graphene: Semiconductor with a Gap Tunable by the Electric Field Effect. *Phys. Rev. Lett.* **2007**, 99, 216802.
43. Zou, K.; Hong, X.; Zhu, J. Effective Mass of Electrons and Holes in Bilayer Graphene: Electron-Hole Asymmetry and Electron-Electron Interaction. *Phys. Rev. B* **2011**, 84, 085408.

44. Li, J.; Tan, L. Z.; Zou, K.; Stabile, A. A.; Seiwell, D. J.; Watanabe, K.; Taniguchi, T.; Louie, S. G.; Zhu, J. Effective Mass in Bilayer Graphene at Low Carrier Densities: The Role of Potential Disorder and Electron-Electron Interaction. *Phys. Rev. B* **2016**, 94, 161406(R).
45. Horng, J.; Chen, C.-F.; Geng, B.; Girit, C.; Zhang, Y.; Hao, Z.; Bechtel, H. A.; Martin, M.; Zettl, A.; Crommie, M. F.; Shen, Y. R.; Wang, F. Drude Conductivity of Dirac Fermions in Graphene. *Phys. Rev. B* **2011**, 83, 165113.
46. Ren, L.; Zhang, Q.; Yao, J.; Sun, Z.; Kaneko, R.; Yan, Z.; Nanot, S.; Jin, Z.; Kawayama, I.; Tonouchi, M.; Tour, J. M.; Kono, J. Terahertz and Infrared Spectroscopy of Gated Large-Area Graphene. *Nano Lett.* **2012**, 12, 3711-3715.
47. Prochaska, L.; Li, X.; MacFarland, D. C.; Andrews, A. M.; Bonta, M.; Bianco, E. F.; Yazdi, S.; Schrenk, W.; Detz, H.; Limbeck, A.; Si, Q.; Ringe, E.; Strasser, G.; Kono, J.; Paschen, S. Singular Charge Fluctuations at a Magnetic Quantum Critical Point. *Science* **2020**, 367, 285-288.
48. Cao, Y.; Chowdhury, D.; Rodan-Legrain, D.; Rubies-Bigorda, O.; Watanabe, K.; Taniguchi, T.; Senthil, T.; Jarillo-Herrero, P. Strange Metal in Magic-Angle Graphene with near Planckian Dissipation. *Phys. Rev. Lett.* **2020**, 124, 076801.
49. Jaoui, A.; Das, I.; Battista, G. D.; Díez-Mérida, J.; Lu, X.; Watanabe, K.; Taniguchi, T.; Ishizuka, H.; Levitov, L.; Efetov, D. K. Quantum Critical Behaviour in Magic-Angle Twisted Bilayer Graphene. *Nat. Phys.* **2022**, 18, 633-638.
50. Martin, J.; Akerman, N.; Ulbricht, G.; Lohmann, T.; Smet, J. T.; Klitzing, K. Von; Yacoby, A. Observation of Electron-Hole Puddles in Graphene Using a Scanning Single-Electron Transistor. *Nat. Phys.* **2008**, 4, 144-148.
51. Ji, Z.; Park, H.; Barber, M. E.; Hu, C.; Watanabe, K.; Taniguchi, T.; Chu, J.-H.; Xu, X.; Shen, Z.-X. Local Probe of Bulk and Edge States in a Fractional Chern Insulator. arXiv: 2404.07157.

Acknowledgements

We acknowledge J. H. Park and J. Kong for sharing their MoS_2 grown by chemical vapor deposition. J.S. acknowledges assistance with handling hydrofluoric acid by V. Kamboj and Y. Wang. This work is funded by NSF DMR-2225925. L.J. acknowledges support from the Sloan Fellowship. J.S. acknowledges support from the Jeollanamdo Provincial Scholarship for Study Overseas. K.W. and T.T. acknowledge support from the JSPS KAKENHI (grant nos. 20H00354, 21H05233 and 23H02052) and World Premier International Research Center Initiative (WPI), MEXT, Japan. This work was carried out in part through the use of MIT.nano's facilities.

Author contributions

L.J. supervised the project. J.S. built the setup with help from Z.L. and F.X. J.S., J.Y., S.Y. and Y.Y. fabricated the devices with help from T.H. and L.S. J.S. performed the THz measurements. K.W. and T.T. grew the hBN crystals. J.S. and L.J. wrote the paper with input from all authors.

Competing interests

The authors declare no competing financial interest.

For Table of Contents Only